Faraday Discussions

Accepted Manuscript

This manuscript will be presented and discussed at a forthcoming Faraday Discussion meeting. All delegates can contribute to the discussion which will be included in the final volume.

Register now to attend! Full details of all upcoming meetings: http://rsc.li/fd-upcoming-meetings

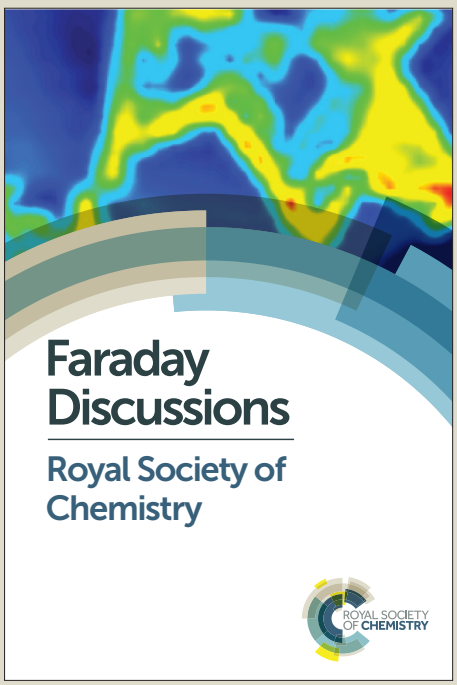

This is an *Accepted Manuscript*, which has been through the Royal Society of Chemistry peer review process and has been accepted for publication.

Accepted Manuscripts are published online shortly after acceptance, before technical editing, formatting and proof reading. Using this free service, authors can make their results available to the community, in citable form, before we publish the edited article. We will replace this *Accepted Manuscript* with the edited and formatted *Advance Article* as soon as it is available.

You can find more information about *Accepted Manuscripts* in the Information for Authors.

Please note that technical editing may introduce minor changes to the text and/or graphics, which may alter content. The journal's standard Terms & Conditions and the Ethical guidelines still apply. In no event shall the Royal Society of Chemistry be held responsible for any errors or omissions in this *Accepted Manuscript* or any consequences arising from the use of any information it contains.

ROYAL SOCIETY OF CHEMISTRY

www.rsc.org/faraday_d

CREATED USING THE RSC REPORT TEMPLATE (VER. 3.1) - SEE WWW.RSC.ORG/ELECTRONICFILES FOR DETAILS
REVIEW Faraday Discussions www.rsc.org/xxxxxx | XXXXXXXX

Dynamical, spectroscopic and computational imaging of bond breaking in photodissociation: roaming and role of conical intersections

Masaaki Nakamura[a], Po-Yu Tsai[a,b], Toshio Kasai[a,c], King-Chuen Lin[a,b], Federico Palazzetti[d,e], Andrea Lombardi[e], Vincenzo Aquilanti[e,f,g]

DOI: 10.1039/b000000x [DO NOT ALTER/DELETE THIS TEXT]

Recent experimental and theoretical advances in the study of dissociation of excited molecules are revealing unexpected mechanisms, when their outcomes are tackled by combining (i) space-time ion imaging of translational features, with (ii) spectroscopic probing of rotational and vibrational distributions; crucial is the assistance by (iii) quantum chemistry of structural investigations of rearrangements of chemical bonds, and by (iv) the simulations of molecular dynamics to follow the evolution of selective bond stretching and breaking. Here we present results of such an integrated approach to methyl formate, $HCOOCH_3$, the simplest of esters; the main focus is on rotovibrationally excited CO (v=1) product and in general on the energy distribution in the fragments. Previous laser studies of dissociation at a sequence of various wavelengths discovered signatures of a roaming mechanism by late arrival in time-of-flight ion imaging of CO (v=0) products. Subsequent detailed investigations as a function of excitation energy provided the assessment of the threshold, which opens for the breakdown in further fragments H and CH_3O, as spectroscopically characterized by ion imaging and FTIR respectively. Accompanying quantum mechanical electronic structure calculations and classical molecular dynamics simulations clarify the origin of these fragments through "roaming" pathways involving incipient radical intermediates at energies below the triple fragmentation threshold: a specific role is played by nonadiabatic transitions at a conical intersection between ground and excited states; alternative pathways focalize our attention to regions of the potential energy surfaces other than those in the neighbourhoods of saddle points along minimum energy paths: eventually this leads to find avenues in reaction kinetics beyond those of venerable transition state theories.

1 Introduction

1. A. Motivation

Following dynamically and spectroscopically the fragments of photodissociated molecules is a technique of choice, whereby in chemistry one can investigate reaction pathways and probe the main features of the involved energy landscapes. According to the Franck-Condon principle applied to molecular photodissociation,

after absorption of photons, molecules access an excited state or a manifold of states, along which they evolve to deliver products carrying the translational and internal energy features due to their experiencing interactions governed by the relevant potential energy surfaces: often systems undergo nonadiabatic transitions back to the ground state without emitting light; the localization of the intersections and the nonadiabatic couplings are key factors to be studied in order to understand the dissociation mechanisms and the effective pathways of molecular fragmentation.

An observed effect that can be attributed to the occurrence of nonadiabatic transitions is the evidence of alternative routes to molecular dissociation that appear to circumvent the minimum energy reaction path: the presence of these alternative pathways can be inferred by the properties of the energy distribution of the product fragments.

A striking feature is provided by roaming pathways that comprise a new class of reaction mechanisms, whose experimental fingerprints are slow and/or internally cold photodissociation products. The roaming atom mechanism has been found to mainly occur in the photodissociation of simple organic molecules (for a review see for example Refs. 1-3 and references therein), e. g. formaldehyde[4], acetaldehyde[5], propionaldehyde[6], methyl formate[7,8], and nitrobenzene[9].

The origin of roaming as a kind of dynamical isomerization or intramolecular rearrangement typically between a weakly bound pair of incipient radicals, is connected to high-lying regions of the electronic ground state surface, corresponding to molecular configurations far from minimum energy paths and transition state geometries. A typical condition for roaming to occur is a pronounced bond elongation up to a partial bond-cleavage in the direction of the dissociation into two radicals (e.g. the C-OCH3 bond of methyl formate), which corresponds to evolution of the system along a high-lying, small gradient region of the potential energy surface. This incipient radical dissociation can end up into the radical product channel, but when the excitation energy is sufficiently high to lead to further dissociation the result is a multiple fragmentation (e. g. triple fragmentation for methyl formate). This common root of roaming and triple fragmentation pathways leads to interchanges of signatures as a function of the excitation energy, a fact amply documented for methyl formate[8] and acetaldehyde[11,12] (see also the discussion on this topic reported in Faraday Discussion 157[10]).

Previous work[8] has emphasized the role of conical intersections of potential energy surfaces as providing a general support for nonadiabatic transitions, channelling the evolution of systems in configurations characterized by highly stretched bonds.

This emerging picture of the roaming phenomenon, in accord with the view of measurable delay in the arrival of product fragment in the molecular channel and their unusual internal rotational energy distribution in CO (v = 0), is corroborated by quantum chemistry and molecular dynamics simulations, exemplified in comparisons extensively sampling initial conditions centred around the transition state and the tip of conical intersection[8]. The experimentally more demanding probes on CO (v = 1), reported and discussed in the following, provide additional insight regarding the vibrational degrees of freedom.

1. B. Plan of the paper

In this paper, the extensive set of the novel measurements on methyl formate photodissociation has been specifically focused at the laser excitation wavelength

value of 248 nm, which has been demonstrated as slightly below the threshold for the triple dissociation into H, CO. and CH_3O. These measurements of the internal energy, and of the images in space and time of the translational features of CO are accompanied by spectroscopic probing of the vibrational and rotational energy deposited in the HCO radical fragment from excited molecules, without however a sufficient energy to further decompose, so to provide clear evidence of the roaming phenomenon, and in general on the internal energy distribution of excited molecules. Previously, photodissociation of methyl formate $HCOOCH_3$ by laser excitation at 234 nm discovered signatures of a roaming mechanism by imaging of CO products[7]: such a mechanism is inferred by late arrival of products in time-of-flight measurements. The subsequent detailed investigations[8], as a function of the excitation energy using a sequence of various laser wavelengths and also the spectroscopic characterization of the fragments H by ion imaging and HCO by Fourier transform infrared spectroscopy (FTIR, see Appendix 1) provided systematic data on the pathways followed by the system for producing radicals and specifically on the threshold for the opening of the breakdown in three fragments. Quantum mechanical electronic structure calculations and classical molecular dynamics simulations clarified the role of both non-adiabatic transitions at a conical intersection of ground state and excited potential energy surfaces.

Focusing on CO (v = 1) from methyl formate dissociation, a clearer signature of roaming is obtained as the bimodal character of the kinetic energy distribution of fragments with respect to the (v = 0) case, where a definite characterization was prevented by the presence of another important mechanisms that generate slow fragments, the CO production by triple fragmentation[10,13].

In this combined experimental and theoretical study of the photodissociation of methyl formate in a subthreshold regime (see Ref. 8) with respect to the triple fragmentation, using laser excitation at 248 nm wavelength, fragmentation into CO and CH_3OH has been characterized by an ion imaging technique, described in Sec. 2. The technique permits vibrational state-specific detection of CO (v): we report probes of population for v=1 vibrational levels for J = 2, 7, and 11 rotational levels. Theoretical approaches are described in Section 3. Available quantum chemical information at the conical intersection and main molecular configurations, particularly at the minimum energy path across the transition state and in the exit channels (molecular and radical, see Ref. 8) are in Sec. 3.A). Sec. 3.B describes how we constructed the ground potential energy surface of the methyl formate and its analytical representation suitable for the classical trajectory simulations. Methods for the latter and for the phase space assessment of triple fragmentation features are given in Sec. 3.B. The results and their distribution are presented in Sec. 4, conclusions follow in Sec. 5. Two appendices provide complementary information on an experimental set up and on theoretical tools: in Appendix A.1, we describe the Fourier transform infrared apparatus; Appendix A.2 provides details on the representation of the ground potential energy surface.

2. Experimental: ion imaging.

The kinetic energy distribution of rotationally and vibrationally selected photofragments of methyl formate (in Section 3.1 we report a description of the dissociative channels) has been measured through an ion imaging technique (see for

example[5,7,14-16] and references therein). The recorded images are two-dimensional projections of three-dimensional distributions with cylindrical symmetry around the photolysis laser polarization axis. The three-dimensional spatial distributions of the fragments were thus reconstructed from the obtained two-dimensional images by efficient deconvolution methods. The speed distributions of the CO fragment were then converted into their corresponding translational energy distributions in the centre-of-mass frame. The imaging results were treated by deconvolution into separate contributions from the various dissociative channels. In this section, we give a detailed description of the experiment performed to probe the vibrationally excited CO (v = 1) fragment (Fig. 1) and show new acquired data for J = 2, 7, and 11 compared with classical trajectory simulation results. The measurements of higher J and CO (v=2) were attempted, but restricted to a poor signal-to-noise ratio. We also recall a previous work on the detection of CO (v = 0) and H fragments. The FTIR technique, employed in accompanying work for the detection of photofragments, is described in Appendix 1.

The photofragment ion images were obtained using a velocity mapping ion imaging apparatus. The methyl formate vapor was premixed with He gas in 10 % concentration. The sample gas was ejected at 900-1000 Torr stagnation pressure through a pulsed valve (General Valve Co.) with 0.6 mm-diameter orifice operating synchronously with the laser pulses at 10 Hz and expanded into the source chamber. After passing through a 1 mm-diameter skimmer and a collimator, the molecular beam was intersected perpendicularly by a linearly polarized laser beam in a two-stage ion lens region. The skimmer was mounted 50 mm downstream from the nozzle to divide the source chamber from the main chamber. A KrF excimer laser (Compex 102, Lambda Physik) emitting at 248 nm with the energy 300-350 μJ/pulse was used as the photolysis source. The laser radiation through an iris was linearly polarized perpendicular to the flight tube and parallel to the detection surface, and then softly focused to the leading edge of the skimmed beam to minimize the cluster formation. A 308 nm XeCl excimer laser (LPX 200, Lambda Physik) -pumped dye laser beam (PD 3000, Lambda Physik) was guided in the opposite direction to probe the CO fragments. Its output was frequency-doubled to emit at ~230 nm with the energy ~180 μJ/pulse. Following the ester photolysis, the focused probe beam was applied in 20 ns delay to detect CO (v=1) by a method of (2+1) resonance-enhanced multiphoton ionization (REMPI) via a $B\ ^1\Sigma^+ \leftarrow X\ ^1\Sigma^+$ two photon transition[17]. Laser pulse powers were adjusted to optimize the two-laser ion signal while minimizing the single-laser ion signal. The resulting CO ions were extracted and accelerated into a 36 cm-length field-free drift tube along the molecular beam direction. The ion-cloud expansion was mapped onto a two-stage microchannel plate and a phosphor screen (FM3040, Galileo). The microchannel plate could be gated within a minimum duration of 90 ns for mass selection. The ion imaging on the phosphor screen was recorded by a charge coupled device camera (200XL4078, Pixelfly). The ion signal intensity was acquired by a photomultiplier tube and a transient digitizer was used to display the time-of-flight mass signal during the experiments.

Methyl formate was photolyzed at 248 nm and the CO (v=1) fragment was probed at selected rotational levels of J=2, 7, and 11. The images at higher J could not be acquired because of the poor signal-to-noise ratio; because of the low resolution especially at low rotational levels, the image at J=2 might be contributed significantly by the adjacent levels. Each image was accumulated up to 30,000-50,000 laser shots. The background images obtained with either photolyzing or

ionizing pulses were both subtracted from raw images to eliminate the contributions from background gases, clusters, and the single-laser ion signal. The production of clusters, present as non-resonant signal in a wide range of ionizing wavelengths, was also carefully minimized in sample preparation and selection of the laser-intercepted region of the molecular beam. The angular distribution of fragments is cylindrically symmetric type around the polarization axis of the photolysis laser beam; the three-dimensional spatial distributions of the fragments can be reconstructed from the obtained two-dimensional images by the basis-set expansion method: all the reconstructed images of CO show an isotropic angular distribution. The velocity distributions of the CO fragment, extracted from the reconstructed ion image, are convoluted to its corresponding translational energy distribution in the centre-of-mass frame. The translational energy profiles were deconvoluted by using Boltzmann-like functions:

$$I_{total} = I_{slow} + I_{fast} = A(E_{CO})^{a_1}[\exp(a_2 E_{CO})] + B(E_{CO})^{b_1}[\exp(b_2 E_{CO})], \quad (1)$$

where the total intensity I_{total} is supposed to be a sum of the intensity of a slow contribution I_{slow} and the intensity of a fast contribution I_{fast}; the explicit form of I_{total} (see Eq. 1) depends on the kinetic energy of CO, E_{CO}, on the weighting factors A and B and on the parameters a_i and b_i (i = 1, 2) that define the profile shape and are also connected to the rotational temperatures of the two distributions.

3. Theoretical tools

In Figure 2, we report a schematic view of the potential energy landscape, for methyl formate ground state S_0: a sketch is given of the minimum energy path, which joins the equilibrium geometry to the molecular products CH_3OH + CO, through a transition state; the figure also gives the feature of a conical intersection that connects the ground state to the excited state surface S_1. (Details on the excited state S_1, on the conical intersection and on the modes excited as the molecule switches from S_0 to S_1 are given in Ref. 18).

3. A. Quantum chemistry and mechanism.

Qualitative features and quantitative assessments of energy and structure of relevant configurations are based on Ref. 18 and private communications by its author, on Refs. 19, 20 and our previous work[7].
We introduce the following dissociative channels:

$HCOOCH_3 + h\nu \rightarrow CH_3OH + CO$, molecular product channel (1)
$HCOOCH_3 + h\nu \rightarrow CH_3O + HCO \rightarrow CH_3O + H + CO$, formyl radical channel (2)
$HCOOCH_3 + h\nu \rightarrow COCH_3O + H$, methoxycarbonyl radical channel (3).

The choice to take into account only the channels (1), (2), and (3) relies on experimental and quantum chemical calculations within the range of excitation energies. The molecular channel (1) (ΔH = ca. 9 kcal/mol, taking into account of the zero point energies of reagent and products) leads to the formation of CH_3OH and CO. It can proceed directly through the minimum energy path (crossing a transition state, ΔH = ca. 68 kcal/mol) or through the roaming mechanism.

The formyl (2) and methoxycarbonyl (3) radical channels can be considered two steps processes, which finally yield the products: CO + H + CH_3O ($COCH_3O$ can further dissociate to CH_3O + CO). The threshold of these triple fragmentation processes have been predicted by quantum chemical calculation: in Channel (2) the first dissociation (formation of CH_3O + HCO products) requires a variation of enthalpy of ca. 97 kcal/mol, while for the final step (dissociation of HCO), ΔH is ca 18 kcal/mol; in the case of methoxycarbonyl radical channel, for the first step ΔH is ca. 100 kcal/mol and for the second step ΔH is ca. 15 kcal/mol; hence, the threshold for both channel (2) and (3) is 115 kcal/mol. Kinematic arguments attribute to channels (2) and (3) rotationally and translationally cold CO products and slow H fragments. It has been argued [8] that channel (3) can be excluded in the probed energy range not only because of an exit energy barrier but also because in configuration space, it lies far away from the configurations considered operative in the present situation. However, our simulations of photodissociation of CO (v=0) indicate that less than 3% of methyl formate dissociates generating methoxycarbonil radicals at 248 nm.

Experimental and theoretical studies on aldehydes [4,5,6] revealed signatures of roaming to the CO product. Evidence is being accumulated that this mechanism typically involves an elongated C – R bonds (where R is H for the formaldehyde, CH_3 for the acetaldehyde and CH_3O for the methyl formate) so that molecules result near dissociated into radicals; the system is in a wide region of the configuration space characterized by a flat potential energy surface, where R abstracts the hydrogen atom from HCO and yields the molecular products (Channel (1)).

In Figures 2 and 3, we show two vectors **r** and **R** (Figure 2), centred in a conical intersection[21] placed close to the product region and pointing along the directions of the H – CO and CH_3O – CO bonds respectively. In such a way, the dissociation process can be illustrated as a three-body event that proceeds through the elongation of the **R** vector: the CH_3O – CO bond length is 0.13 nm for the equilibrium structure of methyl formate, 0.18 nm for the transition state and 0.23 nm for the structure corresponding to the conical intersection, the **r** vector is about 0.10 nm and is almost constant for the three structures, while the H – C – OCH_3 angle is 109° for the equilibrium structure and 49° at the transition state. The simplification to a three-body problem is only for illustration, since in our models we consider also explicitely the internal rotovibration degrees of freedom of CO.

The presence of a conical intersection near the product region at low enough energy, accessible in our experiment, suggests that the formyl radical channel should play a role in the dissociation of methyl formate. A highlight of the potential energy surface referred to the radical channels (channel (2) and channel (3)) after being funnelled through the conical intersection is shown in Figure 3. As mentioned previously, the role of channel (3) can be considered negligible, because its configuration is far from the region of the conical intersection; on the contrary, channel (2) leads to the formation of the radical HCO and CH_3O. Remarkably, the H-C-O angles in the methyl formate ground state minimum and transition state (as obtained from our mode potential energy surface, see Sec. 3.B.) do not differ much, being 136o and 134o respectively, while no such information is available for the conical intersection geometry (the angle is missing in Ref. 18, the sole thoroughly study of methyl formate ground and excited states). If the available energy is enough to overcome the triple dissociation threshold HCO dissociate to yield CH_3O + H + CO, while if the available energy does not allow the system to reach a complete

dissociation, CH_3O remains in the van der Waals region to finally yield the molecular products CH_3OH + CO (roaming mechanism). Our simulations indicate a fraction of 0.15 for the methyl formate molecules that finally dissociate as HCO + CH_30 at 248 nm.

3.B. The Ground State Potential Energy Surface of Methyl Formate.

Available full-dimensional *ab initio* quantum chemical information on methyl formate[18,19] is the starting point to build a reduced four-center ground state potential energy surface suitable for classical trajectory simulations. The reduction consists in taking the CH_3O group as "frozen"; it amounts to consider it as a spectator, possibly available for energy disposal, with the internal energy equally distributed among its degrees of freedom. The potential energy surface of this effective four-center system has been generated in parametric form according to the many-body expansion procedure (see for example Ref. 22), previously applied to several few-body molecules, including formaldehyde, of which the structure HCOH can be thought of as a prototype of the present system (for details of the application of many body expansion on methyl formate see Ref. 23). The potential energy function (available on request) has been constructed with the aid of additional *ab initio* calculations[24]. The same model potential energy surface has been used in simulations presented in Ref. 7. The physically motivated many-body expansion method, used to build the potential energy surface presents definite advantages with respect to the numerical fitting of a huge amount of *ab initio* points calculated on grids. The calculation of accurate single energy point requires a higher level of calculation when compared to the optimization of geometries, adopted in the present method: the calculation of the energy in the long-range region and for bond breaking and formation is in fact critical and requires a very high computational level. The ground state energy curve might also undergo strong coupling with various excited states even at the asymptotic limit. The advantage of this approach is thus to provide an efficient way to generate the global potential energy function with acceptable accuracy for this truncated model system.

The interaction potential of this effective four-body system is given by the following expansion as a sum of n-body contributions (n = 1, 2, 3, 4):

$$V_{\mathrm{HCOM}}=V_{\mathrm{CH}}^{(2)}+V_{\mathrm{CO}}^{(2)}+V_{\mathrm{OH}}^{(2)}+V_{\mathrm{OM}}^{(2)}+V_{\mathrm{HM}}^{(2)}+V_{\mathrm{CM}}^{(2)}+V_{\mathrm{HCO}}^{(3)}+V_{\mathrm{MCO}}^{(3)}+V_{\mathrm{HCM}}^{(3)}+V_{\mathrm{HOM}}^{(3)}+V_{\mathrm{HCOM}}^{(4)}, \quad (2)$$

where the superscripts in parenthesis identifies the n-body interaction terms and subscripts denote the interacting atoms, or the "frozen" CH_3O that hare is referred to as M. The interaction energy at the asymptotic limit of the four single-body terms, $V_{\mathrm{H}}^{(1)}$, $V_{\mathrm{C}}^{(1)}$, $V_{\mathrm{O}}^{(1)}$ and $V_{\mathrm{M}}^{(1)}$, is set tot zero. The force constants for each *n*-body term have been obtained by DFT calculations with B3LYP functional and a 6-311++g(2df,2p) basis set[24].

The interaction potential of 2-body terms $V^{(2)}$, are expressed as Morse potentials whose the parameters can be readily determined via force constants, equilibrium geometries and potential well depths:

$$V^{(2)} = D_e\left[\exp\left(-2a(r-r_e)\right) - 2\exp\left(-a(r-r_e)\right)\right], \quad (3)$$

where $a = \sqrt{\frac{k_e}{\mu}}$

D_e is the dissociation energy, r is the interatomic distance, r_e is the interatomic distance at the equilibrium, k_e is the force constant at the minimum of the potential well and μ is the reduced mass of the two-body term (see Table 1).

The interaction potential of the 3-body terms, $V^{(3)}$ is given in an analytical form:

$$V^{(3)}(R_1, R_2, R_3) = V^0\left(1 + \sum_i C_i\rho_i + \sum_{i\leq j} C_{ij}\rho_i\rho_j + \ldots\right) \times \prod_i\left[1 - \tanh\left(\gamma_i\rho_i/2\right)\right], \quad (4)$$

where $\rho_i = R_i - R_i^{eq}$ and i = 1, 2, and 3. Given the coordinate at equilibrium geometry R_i^{eq} of triatomic fragment ABC, the term V_0 can be calculated by the following expression:

$$V^0 = V_{\mathrm{ABC}}\left(\mathrm{R}_1^{\mathrm{eq}}, \mathrm{R}_2^{\mathrm{eq}}, \mathrm{R}_3^{\mathrm{eq}}\right) - V_{\mathrm{C}}^{(1)} - V_{\mathrm{B}}^{(1)} - V_{\mathrm{A}}^{(1)} - V_{\mathrm{AC}}^{(2)}(\mathrm{R}_3^{\mathrm{eq}}) - V_{\mathrm{AB}}^{(2)}(\mathrm{R}_1^{\mathrm{eq}}) - V_{\mathrm{BC}}^{(2)}(\mathrm{R}_2^{\mathrm{eq}}) \quad (5)$$

where $V_{\mathrm{ABC}}\left(R_1^{\mathrm{eq}}, R_2^{\mathrm{eq}}, R_3^{\mathrm{eq}}\right)$ is the potential of the isolated system ABC and it can be obtained, for example, by *ab initio* calculations; $V_{\mathrm{AC}}^{(2)}(\mathrm{R}_3^{\mathrm{eq}})$, $V_{\mathrm{AB}}^{(2)}(\mathrm{R}_1^{\mathrm{eq}})$, and $V_{\mathrm{BC}}^{(2)}(\mathrm{R}_2^{\mathrm{eq}})$ are the two-body terms introduced in Eq. (3) at the distance of equilibrium of the ABC system. For the specific case of methyl formate (HCOM), ABC corresponds to HCO, HOM, OCM, and HCM.

As done in Ref. 22, we denote the first term at the right hand member of Eq. (4) as expansion function and the second term as switch function. The expression coefficients C_i of the expansion function are correlated to the derivatives of the potential energy (see Appendix 2), R_i are the normal coordinates, $R_i^{eq}$is the equilibrium position of the n-body term, and γ_i, are adjustable parameters in the hyperbolic tangent functions (second term). The divergence of the expansion function at large distance can be compensated by the switch function, which behaves like exponential decay along the coordinates but gives finite value at origin.

The interaction potential of the 4-body term is also expressed in analytic form, not given explicitly here. An example is given in Ref. 22. Further details on the method to obtain the potential energy surface are reported in Appendix 2.

3. C. Classical trajectory simulations

The population CO products in the v=1 vibrational state is expected to be much smaller than the population of CO in the vibrational ground state.

Indeed, in the experiments, the imaging of CO (v=1) required much longer accumulation times than CO(v=0) to obtain reliable results and, at same manner, a consistently large number of trajectories were necessary to obtain an accurate statistical sampling for the CO(v=1) dynamics.

For the theoretical modeling of the photodissociation experiment on CO(v=1), whose results are reported here, around 3 x 10^6 trajectories were run corresponding to a set of given initial geometries of methyl formate. A set of preliminary calculations was performed to establish the best initial geometries, in

which the initial configurations were generated according with the S1/S0 conical intersection configuration of the methyl formate as it is known from Ref. 18, but altering, by a random sampling, the HCO – OCH_3 bond distance to make it varies between 0.21 nm and 0.30 nm. This led us to retain the initial HCO – OCH_3 distance of ca. 0.23 nm as the best initial value for the trajectories. The rest of the initial conditions was generated according to the following scheme: the total internal energy E of the molecule was given a fixed value consistent with the experimental excitation wavelength (115.29 kcal/mol for 248 nm); the initial configuration corresponding to a given potential energy V was assigned to the molecule, and the energy difference (E − V) randomly distributed among the internal degrees of freedom. Trajectories were subjected to the constraint of zero total angular and linear momentum, consistently with the rotationally cold distribution in the beam of molecules to be photoexcited. Alternative initial geometries were also tested, in particular around the minimum energy configuration and the transition state configuration but results were largely not satisfactory, confirming the role of the conical intersection region in the mechanism of the methyl formate photodissociation.

4. Results and discussion.

In Figure 4, we report imaging results of CO (v=1; J= 2, 7, 11). The CO (v = 1) kinetic energy distributions (green curve) are deconvoluted by fitting data into a bimodal Boltzmann function in such a way that deconvoluted different contributions can be disentangled: minimum energy path and roaming. These data are compared with those obtained by classical trajectory simulations. (see right-hand side panels in the figure).

The sharp cold component peaking at 2 kcal/mol (blue curve) is attributed to the roaming process, while the broad component peaking at 5-6 kcal/mol (red curve) is ascribed to the minimum energy path mechanism. The normalized yields of the two mechanisms were evaluated by means of the integrated area of the deconvoluted profiles (see Figure 4); the roaming fraction tends to decrease from 0.29 to 0.17, for J increasing from 2 to 11, while the minimum energy path fraction increases from 0.71 to 0.83. Under the assumption of a Boltzmann distribution, the rotational temperatures of the CO products from each pathway, determined from the J-dependence of the branching fractions, may be approximated to be of 200 K for roaming and for what concerns the molecular channel of 420 K. The total roaming fraction is averaged to 0.2±0.06, as evaluated from the available ratios for J = 2, 7, 11, with the roaming CO product that appear rotationally cold and with a small translational energy. A previous measurement with time-resolved FTIR [25] emission spectroscopy, gave for roaming a rotational temperature of 470 K and for the minimum energy path 1050 K, and a roaming fraction of 0.3±0.04 consistent with the imaging result. The discrepancy of the rotational temperatures could be due to difference in the experimental conditions: the parent molecules are cooled down in the molecular beam experiment, while the FTIR measurements are carried out at room temperature. In addition, the system might not completely reach the thermal equilibrium in the molecular beam, although we assumed the Boltzmann equation to estimate the rotational distribution: CO fragments are ionized in a short time, ca. 20

ns, right after the photolysis laser radiation, while the response time of FTIR measurement ranges to the order of 10^{-6} s.

The results of simulations show a very good qualitative agreement, reproducing bimodality in the kinetic energy distribution of both excited (v = 1) and ground state CO products. Disagreements in the energy range covered by the CO products, which appears to be larger for simulated results. It is probably due to the increased amount of energy available for rotations and translations in our reduced model, where the degrees of freedom of CH_3O group (frozen) are not available for energy disposal.

The v = 1 results can be further discussed with reference to the CO (v = 0) results. In Ref. 8, CO fragments (J = 10, 14, 19, and 24) in their ground vibrational state were obtained by photodissociation at 225, 234, 250, and 255 nm, and probed by ion imaging. The obtained kinetic energy distribution curve appear to be consistent with a bimodal distribution, made up by a slower sharp component and a broad and faster one. Phase space theory calculations and dynamics simulations indicate that at energies above the triple fragmentation threshold (estimated at 248 nm), this channel plays a significant role in contributing to the slow peak in the deconvolution of kinetic energy distribution.

For completeness, we cite results from measurements at higher energies where triple dissociation is open: the kinetic energy distribution of the H atom (see Ref. 8) was measured through ion imaging, for the photodissociation of methyl formate at 243 nm (above the estimated threshold for triple dissociation). In figure 7 of Ref. 8, we reported a fit of the experimental data and the corresponding deconvolution into slow and fast components. The slow component must originate from HCO spontaneous decomposition. According to calculations in Ref. 7, the radical channel lies 97.1 kcal/mol above the methyl formate ground state global minimum energy, while the energy required for dissociation of HCO at its ground electronic state is ca. 17.9 kcal/mol, so we estimate a total available energy of ca. 2.6 kcal/mol, which consistently falls within the experimentally probed range. The broad component is assigned to the two body fragmentation H + $COCH_3O$ (Channel 3, see Sec. 3.A).

5. Conclusions

The exploration of alternative roads that open to molecules with sufficient energy to yield different products is a widely debated subject in the scientific community. An ample discussion on this topic is reported in the proceedings of Faraday Discussion 157, held in Assisi (Perugia, Italy), June 25–27 2012[10], where it was specifically argued by a kinematic approach that slow product fragments can be due to multiple dissociation processes (specifically, triple fragmentation).

In this paper, we reported an overview on the study of photodissociative channels of methyl formate. We presented extensive combined experimental and theoretical studies of methyl formate photodissociation in the 225–255 nm range, where the presence of slow and fast products, which are manifestations of minimum energy path and roaming-mediated mechanisms, established the role of a roaming pathway at these energies. The importance of the triple fragmentation mechanism, whose possible role in the photodissociation of methyl formate was just suggested in the Faraday Discussion 157, has been assessed and it was established a threshold for the opening of the corresponding channel and demonstrated that roaming and triple fragmentation are alternative mechanisms responsible for rotationally and

translationally cold CO products.

We also reported new acquired data on the probe of vibrationally excited CO (v = 1) for excitation energy at 248 nm, slightly lower than the triple fragmentation threshold.

In perspective, a complete study on the photodissociation of methyl formate requires a characterization of the mechanisms also for vibrationally excited molecules. Work in progress using FTIR technique (see Appendix 1) accompanied by computational tools should permit to determine branching ratios and rotational distributions for the various vibrational levels[25].

Appendix 1. Time-resolved Fourier-transform Infrared Emission Spectroscopy.

In this appendix, we report alternative techniques, not employed in the present work to observe evidences of roaming mechanism.

Houston and Kable[26] employed laser-induced fluorescence in the comparable case of the photodissociation of acetaldehyde to CO and CH_4, to resolve the rotational states of the vibrationally selected CO products.

In the photodissociation of methyl formate[8], the Fourier transform infrared (FTIR) emission spectroscopy[27-30] (see the apparatus in Figure 5) was used to probe the formation of HCO fragments. As discussed in Section 4, the presence of a slow peak ascribable to triple fragmentation at 243 nm in the H atom images (see Sec. 3.A for the arguments to exclude Channel (3)) demonstrates that this channel is open at the shorter wavelengths considered in the images of the CO fragments (225 and 240 nm), indicating its contribution to the very sharp and slow peak of the deconvoluted kinetic energy distributions. The threshold for the opening of the triple fragmentation channel (ca. 115 kcal/mol) has been then indirectly confirmed by comparison of the time-resolved FTIR emission spectra of the HCO fragments after photodissociation of methyl formate at 248 nm. The spectrum is compared with the HCO spectrum from the photodissociation of the acetaldehyde at 308 nm and both yielded a similar and consistent decay time, between 5-10 μs, under otherwise identical conditions. In contrast, the acetaldehyde photolysis gives, in the FTIR experiment at 248 nm, an HCO fragment lifetime lower than 5 μs, indicating efficient decomposition. Since the HCO fragment from acetaldehyde photodissociation at 308 nm does not have enough energy to decompose (see Refs. 7, 11 and 12), we conclude that the HCO obtained from methyl formate at 248 nm should not undergo significant decomposition, taking the corresponding irradiation energy value as a threshold for this molecule (115.3 kcal/mol).

Appendix 2. Representation of the ground state Reduced-Dimension Potential Energy Surface of Methyl Formate.

In this appendix, we report details on the method used to build the reduced-dimension potential energy surface of methyl formate, needed for the molecular dynamics simulations.

Force constants. As mentioned in the main text, the required geometric factors and spectroscopic data of isolated 3- and 4- body terms, in internal coordinates (see Table A1-A4) have been obtained by their equilibrium geometries, optimized via DFT method (B3LYP/6-311g(2df,2p)) by using Gaussian03 software. The

relationship between internal coordinates (r_1, r_2, α) and normal coordinates (R_1, R_2, R_3) and the formulas to calculate the force constants are the following:

The calculated harmonic force constant can be expressed in interatomic displacements:

$$\widetilde{V^{(3)}_{\mathrm{MCO}}}(r_1,r_2,a)\equiv V^{(3)}_{\mathrm{MCO}}(R_1,R_2,R_3)=V_{\mathrm{MCO}}(R_1,R_2,R_3)-V^{(2)}_{\mathrm{CM}}(R_1)-V^{(2)}_{\mathrm{CO}}(R_2)-V^{(2)}_{\mathrm{OM}}(R_3)$$

$$f_{\mathrm{ij}}=\left(\frac{\partial^2 V}{\partial R_{\mathrm{i}}\partial R_{\mathrm{j}}}\right)_{\mathrm{eq}},\ F_{\mathrm{ij}}=\left(\frac{\partial^2 \widetilde{V}}{\partial r_{\mathrm{i}}\partial r_{\mathrm{j}}}\right)_{\mathrm{eq}}$$

$$F_{11}=f_{11}+2f_{13}\left(\frac{\partial R_3}{\partial r_1}\right)+f_{33}\left(\frac{\partial R_3}{\partial r_1}\right)^2+\left(\frac{\partial V}{\partial R_3}\right)_{\mathrm{eq}}\left(\frac{\partial^2 R_3}{\partial r_1^2}\right)$$

$$F_{22}=f_{22}+2f_{23}\left(\frac{\partial R_3}{\partial r_2}\right)+f_{33}\left(\frac{\partial R_3}{\partial r_2}\right)^2+\left(\frac{\partial V}{\partial R_3}\right)_{\mathrm{eq}}\left(\frac{\partial^2 R_3}{\partial r_2^2}\right)$$

$$F_{\mathrm{aa}}=f_{33}\left(\frac{\partial^2 R_3}{\partial a^2}\right)+\left(\frac{\partial V}{\partial R_3}\right)^2_{\mathrm{eq}}\left(\frac{\partial^2 R_3}{\partial a^2}\right)$$

$$F_{12}=f_{12}+f_{13}\left(\frac{\partial R_3}{\partial r_2}\right)+f_{23}\left(\frac{\partial R_3}{\partial r_1}\right)+f_{33}\left(\frac{\partial R_3}{\partial r_1}\right)\left(\frac{\partial R_3}{\partial r_2}\right)+\left(\frac{\partial V}{\partial R_3}\right)_{\mathrm{eq}}\left(\frac{\partial^2 R_3}{\partial r_1\partial r_2}\right)$$

$$F_{1\mathrm{a}}=f_{13}\left(\frac{\partial R_3}{\partial a}\right)+f_{33}\left(\frac{\partial R_3}{\partial r_1}\right)\left(\frac{\partial R_3}{\partial a}\right)+\left(\frac{\partial V}{\partial R_3}\right)_{\mathrm{eq}}\left(\frac{\partial^2 R_3}{\partial r_1\partial a}\right)$$

$$F_{2\mathrm{a}}=f_{23}\left(\frac{\partial R_3}{\partial a}\right)+f_{33}\left(\frac{\partial R_3}{\partial r_2}\right)\left(\frac{\partial R_3}{\partial a}\right)+\left(\frac{\partial V}{\partial R_3}\right)_{\mathrm{eq}}\left(\frac{\partial^2 R_3}{\partial r_2\partial a}\right)$$

$$f_{11}=F_{11}$$

$$f_{22}=F_{22}$$

$$f_{33}=\left(F_{33}-\left(\frac{\partial V}{\partial R_3}\right)_{\mathrm{eq}}\left(\frac{\partial^2 R_3}{\partial a^2}\right)\right)\Big/\left(\frac{\partial R_3}{\partial a}\right)^2$$

$$f_{13}=\left(F_{1\mathrm{a}}-\left(\frac{\partial V}{\partial R_3}\right)_{\mathrm{eq}}\left(\frac{\partial^2 R_3}{\partial r_1\partial a}\right)\right)\Big/\left(\frac{\partial R_3}{\partial a}\right)-f_{33}\left(\frac{\partial R_3}{\partial r_1}\right)$$

$$f_{23}=\left(F_{2\mathrm{a}}-\left(\frac{\partial V}{\partial R_3}\right)_{\mathrm{eq}}\left(\frac{\partial^2 R_3}{\partial r_2\partial a}\right)\right)\Big/\left(\frac{\partial R_3}{\partial a}\right)-f_{33}\left(\frac{\partial R_3}{\partial r_2}\right)$$

$$f_{12} = F_{12} - f_{13}\left(\frac{\partial R_3}{\partial r_2}\right) - f_{23}\left(\frac{\partial R_3}{\partial r_1}\right) - f_{33}\left(\frac{\partial R_3}{\partial r_1}\right)\left(\frac{\partial R_3}{\partial r_2}\right) - \left(\frac{\partial V}{\partial R_3}\right)_{\text{eq}}\left(\frac{\partial^2 R_3}{\partial r_1 \partial r_2}\right)$$

The expansion coefficients of the analytical function P (see Eq. (4) and Sec. 3.B) can be evaluated, up to quadratic term at this moment, via the relationship between the coefficients and derivatives of potential. The derivatives of the range function T (see Eq. (4) and Sec. 3.B) can be expressed as:

$$T = [1 - \tanh(\gamma S_{\text{i}}/2)] = 1 - \tanh\left(\gamma\left(R_{\text{i}} - R_{\text{i}}^{\text{eq}}\right)/2\right)$$

$$= 1 - \left(\frac{\text{e}^{\gamma S_{\text{i}}} - 1}{\text{e}^{\gamma S_{\text{i}}} + 1}\right) = \left(\frac{2}{\text{e}^{\gamma S_{\text{i}}} + 1}\right)$$

$$\left(\frac{\partial T^{-1}}{\partial R_{\text{i}}}\right)_{\text{eq}} = \left(\frac{\gamma \text{e}^{\gamma S_{\text{i}}}}{2}\left(\frac{\partial\left(R_{\text{i}} - R_{\text{i}}^{\text{eq}}\right)}{\partial R_{\text{i}}}\right)\right)_{\text{eq}} = \frac{\gamma}{2}$$

The following equation can be treated as the starting point for obtaining the expansion coefficients:

$$\left(\frac{\partial P}{\partial R_{\text{i}}}\right)_{\text{eq}} = \left(V_{\text{ABC}}^{(3)}\frac{\partial T^{-1}}{\partial R_{\text{i}}} + T^{-1}\frac{\partial V_{\text{ABC}}^{(3)}}{\partial R_{\text{i}}}\right)_{\text{eq}} = V_0\frac{\gamma}{2\sqrt{3}} + \left(\frac{\partial V_{\text{ABC}}^{(3)}}{\partial R_{\text{i}}}\right)_{\text{eq}}$$

Analytical forms of coefficients are listed below (up to quadratic terms):

$$g_{\text{i}} = \frac{\gamma}{2}$$

$$G_{\text{ij}} = V_0^{-1}\left(\frac{\partial^2 V_{\text{ABC}}^{(3)}}{\partial R_{\text{i}}\partial R_{\text{j}}}\right)_{\text{eq}} \quad \text{and so on}$$

$$\left(\frac{\partial V_{\text{ABC}}^{(3)}}{\partial R_{\text{i}}}\right)_{\text{eq}} = \left(\frac{\partial V_{\text{ABC}}}{\partial R_{\text{i}}}\right)_{\text{eq}} - \left(\frac{\partial \sum_{\text{j}} V^{(2)}\left(R_{\text{j}}\right)}{\partial R_{\text{j}}}\right)_{\text{eq}} = -\left(\frac{\partial V^{(2)} R_{\text{j}}}{\partial R_{\text{i}}}\right)_{\text{eq}}$$

A. Linear terms:

$$C_{\text{i}} = g_{\text{i}} + G_{\text{i}}$$

$$C_1 = \frac{\gamma_1}{2} - \frac{1}{V_0}\left(\frac{\text{d}V_{\text{AB}}^{(2)}}{\text{d}R_1}\right)_{\text{eq}}, \qquad C_2 = \frac{\gamma_2}{2} - \frac{1}{V_0}\left(\frac{\text{d}V_{\text{BC}}^{(2)}}{\text{d}R_2}\right)_{\text{eq}}, \qquad C_3 = \frac{\gamma_3}{2} - \frac{1}{V_0}\left(\frac{\text{d}V_{\text{AC}}^{(2)}}{\text{d}R_3}\right)_{\text{eq}}$$

Quadratic terms

$$C_{ii}=g_i^2+g_i G_i+G_{ii}/2$$

$$C_{ij}=g_i g_j+g_i G_j+g_j G_i+G_{ij}$$

$$C_{11}=\frac{\gamma_1^2}{4}-\left(\frac{\gamma_1}{2V_0}\right)\left(\frac{\partial V_{CM}^{(2)}}{\partial R_1}\right)_{eq}+\left(f_{11}-\left(\frac{\partial^2 V_{CM}^{(2)}}{\partial R_1^2}\right)_{eq}\right)\Big/2V_0$$

$$C_{22}=\frac{\gamma_2^2}{4}-\left(\frac{\gamma_2}{2V_0}\right)\left(\frac{\partial V_{CO}^{(2)}}{\partial R_2}\right)_{eq}+\left(f_{22}-\left(\frac{\partial^2 V_{CO}^{(2)}}{\partial R_2^2}\right)_{eq}\right)\Big/2V_0$$

$$C_{33}=\frac{\gamma_3^2}{4}-\left(\frac{\gamma_3}{2V_0}\right)\left(\frac{\partial V_{OM}^{(2)}}{\partial R_3}\right)_{eq}+\left(f_{33}-\left(\frac{\partial^2 V_{OM}^{(2)}}{\partial R_3^2}\right)_{eq}\right)\Big/2V_0$$

$$C_{12}=\frac{\gamma_1\gamma_2}{4}-\left(\frac{1}{2V_0}\right)\left[\gamma_1\left(\frac{\partial V_{CM}^{(2)}}{\partial R_1}\right)_{eq}+\gamma_2\left(\frac{\partial V_{CO}^{(2)}}{\partial R_2}\right)_{eq}\right]+\frac{f_{12}}{V_0}$$

$$C_{13}=\frac{\gamma_1\gamma_3}{4}-\left(\frac{1}{2V_0}\right)\left[\gamma_1\left(\frac{\partial V_{CM}^{(2)}}{\partial R_1}\right)_{eq}+\gamma_3\left(\frac{\partial V_{OM}^{(2)}}{\partial R_3}\right)_{eq}\right]+\frac{f_{13}}{V_0}$$

$$C_{23}=\frac{\gamma_2\gamma_3}{4}-\left(\frac{1}{2V_0}\right)\left[\gamma_2\left(\frac{\partial V_{CO}^{(2)}}{\partial R_2}\right)_{eq}+\gamma_3\left(\frac{\partial V_{OM}^{(2)}}{\partial R_3}\right)_{eq}\right]+\frac{f_{23}}{V_0}$$

The evaluated coefficients are listed in Tables A1-A4. Note that in all the 3-body terms, none of them has multiminima except the term for HCO. H can attach to either the O-atom end or C-atom end. Due to limited amount of data, the expansion coefficients are evaluated up to quadratic terms.

After obtaining the 3-body and 4-body force constants from *ab initio* calculations or literature data, the undetermined parameters (γ) can be optimized by following the steps reported below:

(i) initial values of γ in the 3-body terms are chosen according to *ab initio* 3-body interaction energies and geometries;

(ii) the γ parameters of the 3-body terms are adjusted manually according to the *ab initio* 4-body geometry and behaviour of radical dissociation channels HCOM → HCO+M and HCOM → H+COM;

(iii) the γ parameters of the 3-body terms are optimized according to the *ab initio* 4-body geometry (without the 4-body term)

(iv) γ of the 4-body term optimized according to *ab initio* 4-body interaction energy and geometry (with γ of 3-body terms fixed).

According to the *ab initio* calculations, the four atoms are placed within a plane at the equilibrium geometry and such geometrical constraint has been considered during the optimization of the adjustable parameters. Besides, note that although the expansion coefficients of the HCO 3-body term have already been refined by optimizing the adjustable parameter γ, these are treated as adjustable variables again without changing the expansion coefficients themselves, in order to obtain a better optimization for the HCOM geometry and the global minimum. The refined γ's of

HCO 3-body terms are γ_1 (CH) =, γ_2 (CO) = 1.255612, and γ_3 (OH) = 1.843658.
The relative displacements (in nm) of the optimized geometry of the potential energy surface and the corresponding *ab initio* values (in parenthesis) are as follows: CH = 0.10693 (0.10967); CM = 0.13361 (0.13372); CO = 0.12495(0.11993); OH=0.20451(0.20366); OM = 0.23045(0.22599); HM = 0.1981(0.19883).
The averaged error is around 0.0025 nm and corresponds to a mean relative error of 1.6 %. Angles (in degrees) of the OCH, HCM and OCM bonds are 123.5753 (124.9), 110.395(109.2) and 126.03(125.9), respectively. The global minimum energy related to the asymptotic limit of the four bodies is -16.5418 eV, while the *ab initio* value is -16.51 eV.

Acknowledgments

The work carried out in Taiwan is supported by Ministry of Science and Technology, Taiwan, Republic of China under contract no. NSC 102-2113-M-002-009-MY3. T. Kasai is grateful to the Ministry of Science and Technology, for supporting his stay at the Department of Chemistry, National Taiwan University. A. Lombardi acknowledges financial support from MIUR PRIN 2010-2011 (con- tract 2010ERFKXL 002) and EGI Inspire. Thanks are also due to IGI (Italian Grid Infrastructure) and COMPCHEM Virtual Organization for the allocated computing time." V.A. acknowledges CAPES (Brazil) for the position of Pesquisador Visitante Especial at UFBA.

References

[a] *Department of Chemistry, National Taiwan University, Taipei 106, Taiwan.Tel: +886 2 33661162; Fax: +886 2 23621483, E-mail: kclin@ntu.edu.tw*
[b] *Institute of Atomic and Molecular Sciences, Academia Sinica, Taipei 106, Taiwan.*
[c] *Graduate School of Science, Department of Chemistry, Osaka University, Toyonaka, 560-0043 Osaka, Japan*
[d] *Scuola Normale Superiore, 56126 Pisa, Italy.*
[e] *Dipartimento di Chimica, Biologia e Biotecnologie, Università di Perugia, 06123 Perugia, Italy. Tel: +39 075 5855512; Fax: +39 075 5855606; E-mail: vincenzoaquilanti@yahoo.it*
[f] *Consiglio Nazionale delle Ricerche, Istituto di Metodologie Inorganiche e dei Plasmi, 00016 Roma, Italy.*
[g] *Instituto de Física, Universidade Federal da Bahia, 40210 Salvador, Brazil*
† See DOI: 10.1039/b000000x/

1 J. M. Bowman, Mol. Phys. 10.1080/00268976.2014.897395
2 T. Kasai, D. –C. Che, M. Okada, P. –Y. Tsai, K. –C. Lin, F. Palazzetti, V. Aquilanti, *Phys. Chem. Chem. Phys.* 2014 **16** 9776-9790.
3 A. G. Suits, Acc. Chem. Res., 2008, 41, 873 .
4 D. Townsend, S. A. Lahankar, S. K. Lee, S. D. Chambreau, A. G. Suits, X. Zhang, J. Rheinecker, L. B. Harding and J. M. Bowman, Science, 2004, 306, 1158
5 K. –C. Hung, P. –Y. Tsai, H. –K. Li, K. –C. Lin, J. Chem. Phys. 2014, 140, 064313.
6 P. –Y. Tsai, K. –C. Hung, H. –K. Li, and K. –C. Lin, J. Phys. Chem. Lett. 2014, 5, 190-195.
7 M. H. Chao, P. Y. Tsai, and K. C. Lin, Phys. Chem. Chem. Phys., 2011, 13, 7154.
8 P. –Y. Tsai, M. –H. Chao, T. Kasai, K. –C. Lin, A. Lombardi, F. Palazzetti, V. Aquilanti, Phys. Chem. Chem. Phys. 2014, 16, 2854-2865.
9 M. L. Hause, N. Herath, R. Zhu, M. C. Linand and A. G. Suits, Nat. Chem., 2011, 3, 932
10 Molecular Reaction Dynamics in Gases, Liquids and Interfaces, Faraday Discuss., 2012, p. 157, Assisi (Perugia, Italy).
11 L. Rubio-Lago, G. A. Amaral, A. Arregui, G. A. Amaral, A. Arregui, L. Rubio-Lago, J. D. Rodríguez and L. Bañares, Phys. Chem. Chem. Phys., 2010, 133, 64303
12 L. Rubio-Lago, G. A. Amaral, A. Arregui, J. Gonzalez-Vazquez and L. Banares, Phys. Chem. Chem. Phys., 2012, 14, 6067 RSC .
13 G. de Wit, B. R. Heazlewood, M. S. Quinn, A. T. Maccarone, K. Nauta, S. A. Reid, M. J. T. Jordan and S. H. Kable, Faraday Discuss., 2012, 157, 227.
14 T. J. B. Eppink and D. H. Parker, Rev. Sci. Instrum., 1997, 68, 3477 .
15 Y. Tang, W. B. Lee, Z. F. Hu, B. Zhang and K. C. Lin, J. Chem. Phys., 2007, 126, 064302
16 X. P. Zhang, W. B. Lee, D. F. Zhao, M. K. Hsiao, Y. L. Chen and K. C. Lin, J. Chem. Phys., 2009, 130, 214305.
17 M. Castillejo, S. Couris, E. Lane, M. Martin and J. Ruiz, Chem. Phys., 1998, 232, 353
18 G. Cui, F. Zhang and W. Fang, J. Chem. Phys., 2010, 132, 034306.

19 J. S. Francisco, J. Am. Chem. Soc., 2003, 125, 10475.
20 S. H. Lee, J. Chem. Phys., 2008, 129, 194304.
21 M. Baer, Beyond Born–Oppenheimer: Electronic Nonadiabatic Coupling Terms and Conical Intersections, 2006John Wiley & Sons, Hoboken, NJ, USA .
22 J. N. Murrell, S. Carter, S. C. Farantos, P. Huxley and A. J. C. Varandas, Molecular potential energy functions, 1984, John Wiley & Sons, London.
23 A. Lombardi, F. Palazzetti, K. –C. Lin, P. –Y. Tsai, Lecture Notes in Computer Science (including subseries Lecture Notes in Artificial Intelligence and Lecture Notes in Bioinformatics),2014, 8579 LNCS (PART 1), pp. 452-467
24 GAUSSIAN 03, Revision C.02, 2004Gaussian, Inc., Wallingford, CT.
25 M. Nakamura, P. –Y. Tsai, T. Kasai, K. –C. Lin, F. Palazzetti, A. Lombardi, V. Aquilanti. In Preparation.
26 P. L. Houston and S. H. Kable, Proc. Natl. Acad. Sci. U. S. A., 2006, 103, 16079.
27 Y. T. Liu, M. T. Tsai, C. Y. Liu, P. Y. Tsai, K. C. Lin, Y. H. Shih and A. H. Chang, J. Phys. Chem. A, 2010, 114, 7275 .
28 Y. Y. Yeh, M. H. Chao, P. Y. Tsai, Y. B. Chang, M. T. Tsai and K. C. Lin, J. Chem. Phys., 2012, 136, 044302 .
29 R. A. Palmer, J. L. Chao, R. M. Dittmar, V. G. Gregoriou and S. E. Plunkett, Appl. Spectrosc., 1993, 47, 1297 .
30 G. V. Hartland, W. Xie, H. L. Dai, A. Simon and M. J. Anderson, Rev. Sci. Instrum., 1992, 63, 3261 .

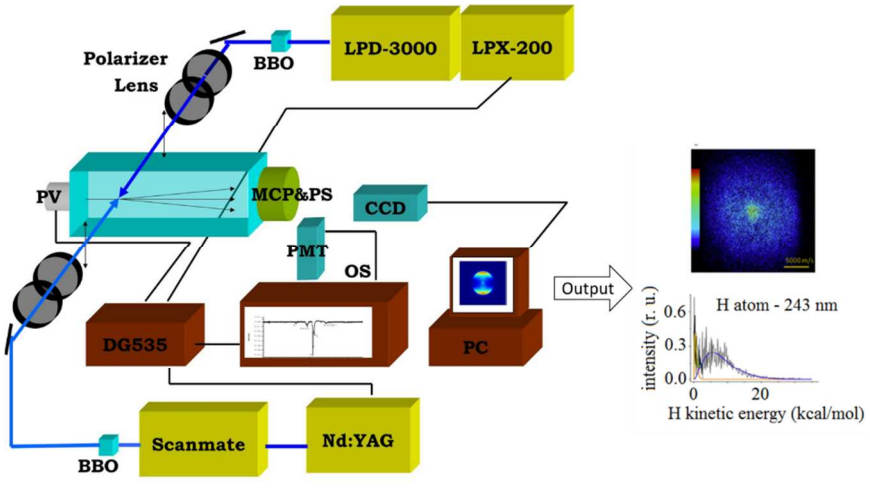

Fig. 1. Experimental apparatus for measurements of velocity mapping ion imaging. A Nd:YAG laser pumped dye laser operating with different laser dyes is used as photolysis source, its output frequency is doubled by a BBO (β-barium borate) crystal. A 308 nm XeCl excimer laser (Lambda Physics LPX-200) pumping dye laser beam (LPD-3000) is guided in the opposite direction to probe the fragments (in the present case CO). Also in this case, the output is frequency-doubled to emit at the requested wavelength and to ionize the product. The reactant precursor (in this case methyl formate) is prepared in helium-seed free-jet molecular beam (PV = pulse valve), the photofragments are then produced and ionized in laser-molecular beam intersection region at downstream. The ion-cloud expansion is mapped onto a two-stage microchannel plate (MCP) and a phosphor screen (PS), then recorded by a charge coupled device (CCD) camera. All the ion signals without gate restriction are acquired by a photomultiplier tube (PMT) and transferred to a transient digitizer to display the time-of-flight mass spectrum. Results are displayed by an oscilloscope (OS) and a personal computer (PC). 2-dimensional image of H atom and its deconvoluted plot, which permits to obtain the kinetic energy distribution of the photofragment, are shown in the panels in the right. (Adapted from Ref. 7).

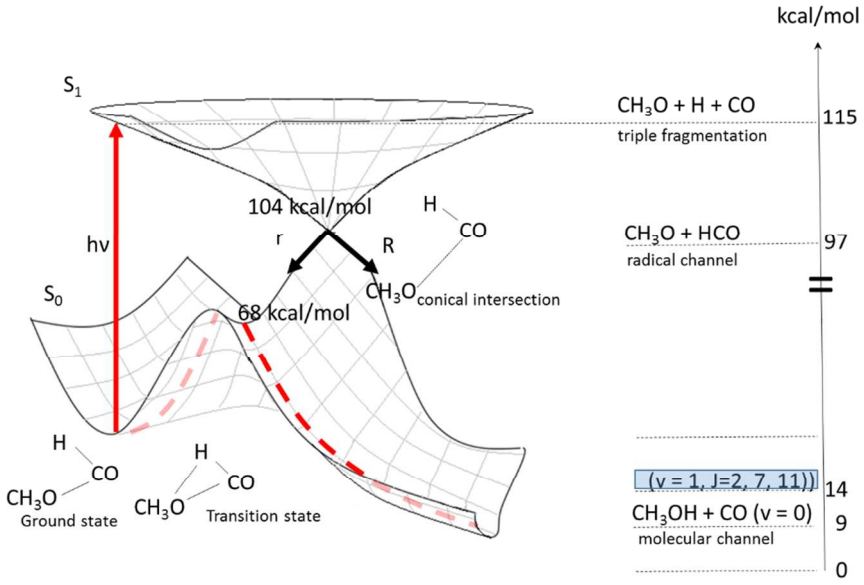

Fig. 2. A schematic view of the photodissociation pathways of methyl formate. The minimum energy path, from the ground state to the dissociated products CH_3OH + CO passing through the transition state, is represented by the red-dashed line. From the ground state (S_0), the molecule is promoted to the excited state (S_1) through laser excitation at 248 nm. The very large vibronic coupling induces the transition to the ground state through the conical intersection giving CH_3OH + CO products, while the triple dissociation channel, which yields CH_3O + CO + H, is not accessible because its threshold is slightly higher than the energy provided by the laser. Vectors **r** and **R**, centered at the conical intersections, for illustration are shown pointing in the direction of the H – CO and of the CH_3O – CO, respectively. In the ground state, **r** = 0.11 nm and **R**=0.13 nm ca.; at the transition state **r** = 0.11nm and **R**=0.18 nm ca.; at the conical intersection **r** = 0.11 nm and **R**=0.23 nm ca.. The latter values corroborate the view that the main radical path responsible for the observed for roaming originates from the elongation of the CH_3O – CO bond.

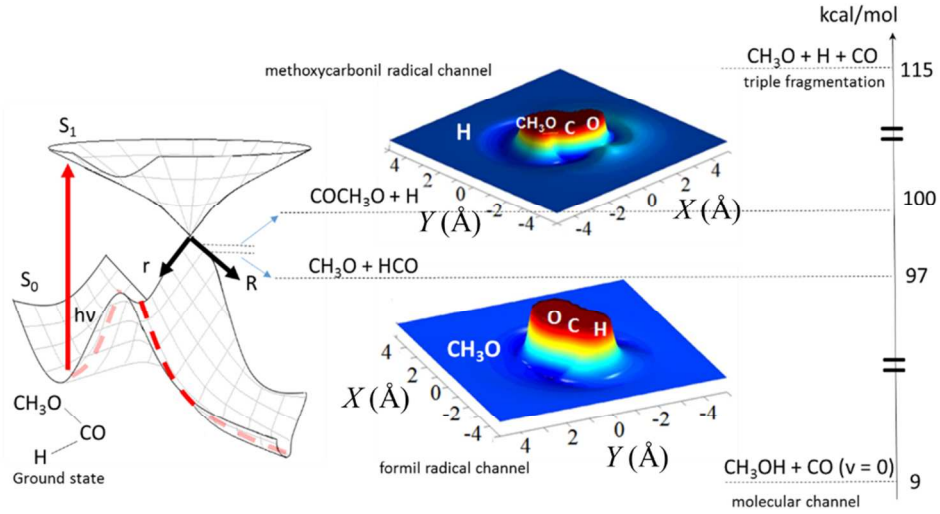

Fig. 3. We report a detail of the methoxycarbonyl and formyl radical channels. The illustrative tridimensional plots (in the right-hand side) show the interaction of H+$COCH_3O$ and CH_3O+HCO as reduced three-body problems (the internal degrees of freedom of CO and of CH_3O being considered as frozen); the origin of the Cartesian coordinates in each plot is the center of mass of the triatomic fragment, and the CO vector points in the positive direction of *x*-axis. The geometry of each triatomic fragment is fixed at the equilibrium structure of $HCOOCH_3$, and the interaction energy (in kcal/mol) is taken with respect to the four-body dissociation (H+C+O+CH_3O) as zero. In the methoxycarbonyl radical channel, the **r** vector varies and the **R** vector is fixed (see Figure 2), while *viceversa* in the formyl radical channel case. This latter case corresponds to the elongation of the CO – CH_3O bond, a situation which occurs in the structure of methyl formate at the conical intersection.

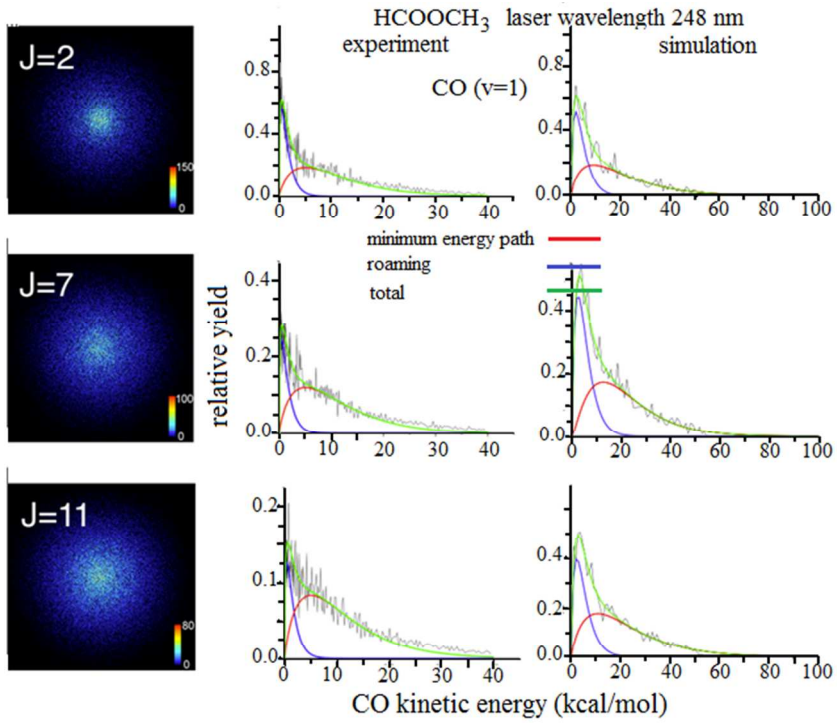

Fig. 4. The figure shows the image (left panels) and the extracted kinetic energy distributions of vibrational excited CO (v = 1) from photodissociation of methyl formate at 248 nm, for the selected rotational levels J = 2, 7, and 11. In central panels, fits of the experimental data (green curve) and deconvolution of slow (in blue) and fast (in red) components are reported. Panels in the right-hand side show the corresponding results as obtained by classical trajectory simulations. The normalized yields by the integration of the area of the deconvoluted profiles (central panels) are: for the roaming mechanism, 0.29 ± 0.07 for J = 2, 0.20 ± 0.09 for J = 7, and 0.17 ± 0.04 for J = 11. For the minimum energy path mechanism, 0.71 ± 0.12 for J = 2; 0.80 ± 0.20 for J = 7, and 0.83 ± 0.08 for J = 11.

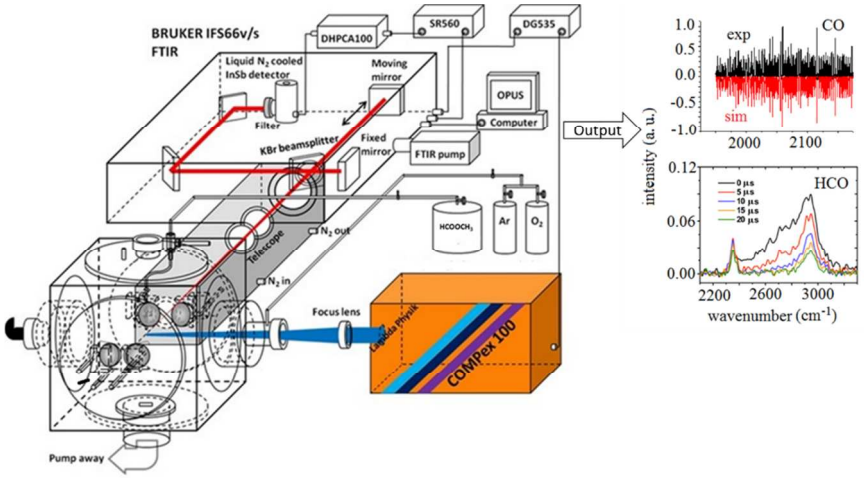

Fig. 5. Experimental apparatus for FTIR emission measurements. The photodissociation source is a KrF excimer laser (Lambda Physik COMPex 100); the incident UV laser beam is focused into stainless steel gas chamber with a spherical lens. The reactant precursor (in this case methyl formate) flows into chamber along an inlet intruding from the top of the chamber, while the Ar or O_2 collision partners are injected close to the end window on the chamber. The fragment emission signals are collected in perpendicular direction to laser beam via a nitrogen-purged light path which is composed of a pair of focal lens (telescope). The IR emission light is introduced into FT-IR spectrometer (IFS 66v/S, Bruker). The transmitted signal is monitored with an InSb detector cooled at 77 K, the obtained interferograms can be Fourier transformed to give rise to a series of time-resolved spectra via OPUSTM software. DHPCA100: DHPCA100 current preamplifier. SR560: voltage preamplifier (Stanford Research Systems, SR560). DG535: time-delay generator(Stanford Research Systems, DG535). As example of output, we report (right panels) the spectra with different resolution of CO and HCO fragments.

Table 1. Morse parameters for 2-body terms.

	C-O	C-M	O-M	C-H	O-H	M-H
D_e (eV)	11.224	3.959	2.231	3.648	4.632	4.477
r_e (nm)	0.113	0.134	0.132	0.112	0.097	0.095
k_e (a. u.)	2.4649	0.233	0.451	0.330	0.555	0.567

Table A.1. The expansion coefficients of MCO 3-body term (distances are in nm, energies in eV, force constants of internal coordinate in au].

MCO	V_0	C_1	C_2	C_3
	3.033	1.978804	5.689299	1.341308
	C_0	C_{11}	C_{22}	C_{33}
	1.0	5.840956	42.290240	7.390537
R_{eq1}(CM)	γ_1	C_{12}	C_{13}	C_{23}
1.32747	3.796384	14.924260	4.628371	8.436104
R_{eq2}(CO)	γ_2	F_{11}	F_{22}	F_{aa}
1.17985	17.742849	0.375867	0.921841	0.307491
R_{eq3}(OM)	γ_3	F_{12}	F_{1a}	F_{2a}
2.25006	3.151990	0.106342	0.0610	0.048397

Table A.2. The expansion coefficients of the HOM 3-body term (distances are in nm, energies in eV, force constants of internal coordinate in au).

HOM	V_0	C_1	C_2	C_3
	0.1733	-4.307835	1.369019	2.123089
	C_0	C_{11}	C_{22}	C_{33}
	1.0	9.491546	-13.384507	22.562432
R_{eq1}(OM)	γ_1	C_{12}	C_{13}	C_{23}
2.20174	0.854314	-2.215224	-35.588642	3.303192
R_{eq2}(OH)	γ_2	F_{11}	F_{22}	F_{aa}
0.96919	1.602842	0.015698	0.5108	0.01715
R_{eq3}(HM)	γ_3	F_{12}	F_{1a}	F_{2a}
2.3398	12.218217	0.00177	-1.34873	-0.003325

Table A.3. The expansion coefficients of HCM 3-body term (distances are in nm, energies in eV, force constants of internal coordinate in au).

HCM	V_0	C_1	C_2	C_3
	0.2223	3.793969	7.558600	-3.578366
	C_0	C_{11}	C_{22}	C_{33}
	1.0	51.922756	-11.434842	42.887273
R_{eq1}(CM)	γ_1	C_{12}	C_{13}	C_{23}
1.3197	3.691497	77.886641	-66.760355	-60.012112
R_{eq2}(CH)	γ_2	F_{11}	F_{22}	F_{aa}
1.08078	2.315571	0.46092	0.3270	0.1952
R_{eq3}(HM)	γ_3	F_{12}	F_{1a}	F_{2a}
2.12	3.298011	0.141	-0.14488	-0.15186

Table A.4. The expansion coefficients of HCOM 4-body interaction term (distances are in nm, energies in eV, force constants of internal coordinate in au).

HCOM	V_0	C_1	C_2	C_3
	-0.606778	9.945154	17.127433	55.888183
	C_0	C_4	C_5	C_6
	1.0	-20.358639	2.354528	-8.842246
R_{eq1}(CH)	γ_1	C_{11}	C_{22}	C_{33}
1.096720	17.187900	59.811865	147.350834	1199.089874
R_{eq2}(CM)	γ_2	C_{44}	C_{55}	C_{66}
1.33720	18.029200	197.839527	-14.560888	22.429016
R_{eq3}(CO)	γ_3	C_{12}	C_{13}	C_{14}
1.199260	36.923900	132.489306	454.087857	-139.150904
R_{eq4}(CM)	γ_4	C_{15}	C_{16}	C_{23}
2.036620	-22.909700	18.663936	-59.772061	619.211472
R_{eq5}(OM)	γ_5	C_{24}	C_{25}	C_{26}
2.259870	-8.012290	-264.525530	36.965650	-70.453209
R_{eq6}(HM)	γ_6	C_{34}	C_{35}	C_{36}
1.988260	-2.651190	-761.097790	-70.045682	-202.258401
		C_{45}	C_{46}	C_{56}
		-14.482735	-87.086552	11.589886
F_{11}	F_{22}	F_{33}	F_{44}	F_{55}
0.33613	0.16776	0.31924	-0.32005	-2.3977e-2
F_{66}	F_{12}	F_{13}	F_{14}	F_{15}
-0.11238	0.49588	0.21452	-7.445e-2	-0.30104
F_{16}	F_{23}	F_{24}	F_{25}	F_{26}
-0.12487	0.70676	-0.27129	-0.22727	-6.6139e-2
F_{34}	F_{35}	F_{36}	F_{45}	F_{46}
0.36027	1.4466e-1	2.89012e-1	0.33168	9.61107e-2
F_{56}				
0.17254				

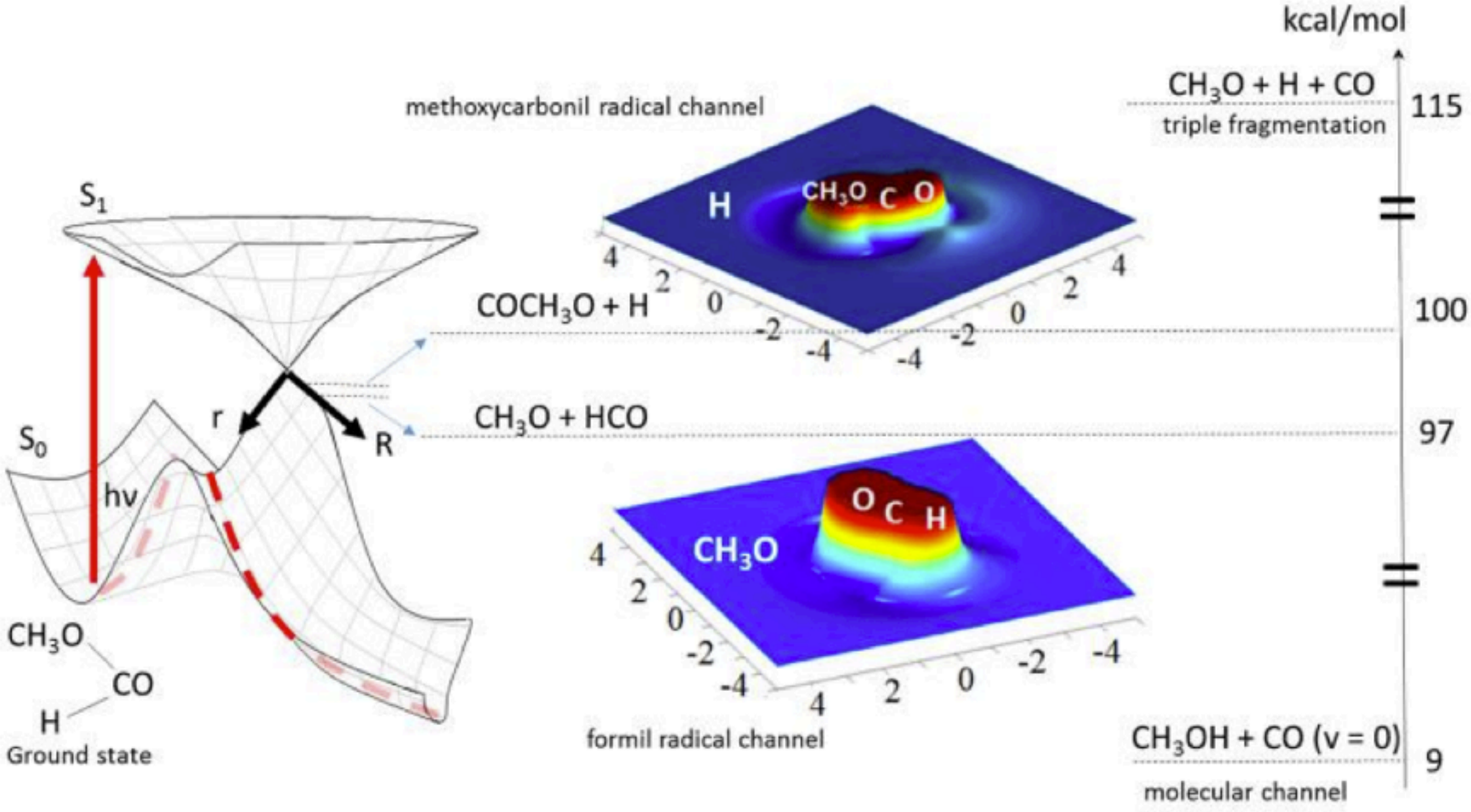

Probing alternative routes to dissociation of molecules in space and time.